Theoretical and Applied Climatology (2024) 155:859–877
https://doi.org/10.1007/s00704-023-04663-2

ORIGINAL PAPER

Effect of atmospheric conditions and VPRM parameters on high-resolution regional CO_2 simulations over East Asia

Min-Gyung Seo[1] · Hyun Mee Kim[1] · Dae-Hui Kim[1]

Received: 18 February 2022 / Accepted: 17 September 2023 / Published online: 3 October 2023

Abstract

Atmospheric CO_2 concentrations are largely affected by the surface CO_2 flux and atmospheric wind. To estimate atmospheric CO_2 concentrations over East Asia, the effects of atmospheric conditions and the parameters of Vegetation Photosynthesis and Respiration Model (VPRM) that simulates biogenic CO_2 concentrations were evaluated using the Weather Research and Forecasting model coupled with Chemistry (WRF-Chem) model. The VPRM in WRF-Chem requires parameter optimization for the experimental period and region. Total six experiments with two atmospheric fields (final analysis; FNL and fifth generation of European Centre for Medium-range Weather Forecasts atmospheric reanalysis; ERA5) and three VPRM parameter tables (US, Li, and Dayalu) were conducted to investigate the appropriate atmospheric field and VPRM parameter table for East Asia. For validation, two types of wind observations (SYNOP and SONDE) and two types of CO_2 observations (surface CO_2 observations and OCO-2 XCO_2 observations) were used. The experiments using FNL showed a lower RMSE for surface winds, whereas those using ERA5 showed a lower RMSE for upper-air winds. On average, the surface wind RMSE in the experiments using FNL was lower than that using ERA5. With respect to surface CO_2 observations, the experiments using the Li table showed relatively lower RMSEs compared to those using other tables. With respect to OCO-2 XCO_2 observations, the Li table with FNL showed lower RMSEs than other combinations. Overall, the combination of the Li table and FNL was the most appropriate for simulating CO_2 concentrations in East Asia using WRF-Chem with VPRM.

1 Introduction

Atmospheric CO_2 concentrations have increased more than 50% compared to those pre-industrialization due to increasing fossil fuel consumption (Friedlingstein et al. 2022). Various efforts have been made to reduce global warming induced by CO_2 emissions. The Kyoto Protocol of the United Nations Framework Convention on Climate Change) (UNFCCC), adopted on December 11, 1997, aims to reduce the emissions of six types of greenhouse gases, including CO_2 (unfccc.int/process-and-meetings/the-kyoto-protocol/what-is-the-kyoto-protocol/). The Paris Agreement, adopted on December 12, 2015, aims to keep the global average temperature increase within 2 °C of that before industrialization by reducing CO_2 emissions (unfccc.int/process-and-meetings/the-paris-agreement). Although East Asia is the third-largest source region of CO_2 after North America and Europe, the number of surface CO_2 observations in East Asia is relatively small compared to that in North America and Europe (Moran et al. 2018), which makes the estimation of surface CO_2 fluxes in East Asia highly uncertain (Stephens et al. 2007).

To decrease the uncertainties associated with surface CO_2 flux estimation in East Asia, many studies have been conducted using various models. Jing et al. (2018) simulated global CO_2 concentrations using the Goddard Earth Observing System Chemistry (GEOS-Chem) model and compared them with observed column-averaged CO_2 (XCO_2) concentrations of Greenhouse Gases Observing Satellite (GOSAT) and total carbon column observing network (TCCON). CarbonTracker, developed by the National Oceanic and Atmospheric Administration (NOAA) Earth System Research Laboratory (ESRL), has also been used to estimate surface CO_2 fluxes over East Asia and globe (Kim et al. 2014a, 2014b, 2017, 2018; Park and Kim 2020; Cho and Kim 2022). Although a nesting domain is used for more detailed simulations of CO_2 flux or concentrations over East Asia using global models (i.e., GEOS-Chem and CarbonTracker)

✉ Hyun Mee Kim
khm@yonsei.ac.kr

1 Atmospheric Predictability and Data Assimilation Laboratory, Department of Atmospheric Sciences, Yonsei University, Seoul 03722, Republic of Korea

(Shim et al. 2013; Kim et al. 2014a), it is difficult to produce high-resolution simulations at a regional scale using global models because of limitations in resolution size and computational resources. Therefore, studies using regional models (e.g., Community Multiscale and Air Quality (CMAQ) model and the Weather Research and Forecasting model coupled with Chemistry (WRF-Chem) have been conducted to simulate high-resolution CO_2 concentrations. CMAQ is an offline model that performs chemical forecasts using atmospheric fields as an input, whereas WRF-Chem is an online model that simultaneously conducts atmospheric and chemical forecasts. Li et al. (2017) simulated the CO_2 concentration in East Asia using the CMAQ and compared the results with observed XCO_2 concentrations of GOSAT. Dong et al. (2021) simulated the CO_2 concentrations in China using the WRF-Chem and diagnosed the spatial and temporal variations of CO_2. Zheng et al. (2019) compared the XCO_2 concentrations produced by WRF-Chem with those produced by Orbiting Carbon Observatory 2 (OCO-2) to evaluate CO_2 emissions from power plants located in the United States (US). To evaluate the most suitable setup in the WRF-Chem to simulate CO_2 concentrations in the US, sensitivity experiments for physical processes and CO_2 emission inventory have been performed (Martin et al. 2019; Feng et al. 2016, 2019).

Among the regional models, WRF-Chem considers the interactions between atmospheric variables and chemical components as the interactions occurred in the real atmosphere. To simulate the high-resolution regional CO_2 concentrations using WRF-Chem, several components including the emission inventories, atmospheric initial and boundary conditions, initial and boundary conditions of CO_2, and physical parameterizations in WRF-Chem need to be considered. For the emission inventory, anthropogenic and oceanic CO_2 concentrations can be provided from each emission inventory data. Initial and boundary conditions of CO_2 can be provided by the global models such as GEOS-Chem and CarbonTracker. For the physical parameterizations in WRF-Chem, Díaz-Isaac et al. (2018) investigated the impact of physical parameterizations and initial conditions on simulated CO_2 concentrations in the US.

For the biogenic CO_2 concentration, the Vegetation Photosynthesis and Respiration Model (VPRM) combined with WRF-Chem can be used. The VPRM is a model that calculates gross ecosystem exchange (GEE) and respiration (R) to simulate biogenic CO_2 concentrations (Ahmadov et al. 2007). To calculate the GEE and R in the VPRM, four parameter values are required (Mahadevan et al. 2008), which should be optimized for the experimental area (Hilton et al. 2013). The parameters of the VPRM model need to be optimized using eddy-covariance observations for each vegetation type present in the experimental region (Mahadevan et al. 2008). The VPRM parameters optimized for the US, Europe, and tropical regions are provided in WRF-Chem. Several studies have attempted to optimize parameters for their experimental region. Park et al. (2018) performed parameter optimization for the downtown area of California, USA, and Hilton et al. (2013) performed parameter optimization in North America. In East Asia, Dayalu et al. (2018) performed parameter optimization for 2005–2009 using eddy-covariance observations for the same period in China and Korea. Li et al. (2020) suggested using the VPRM parameter table modified from Hilton et al. (2013) for northeastern China and analyzed the uncertainties related to parameters for northeastern China. Park et al. (2020) simulated CO_2 with a VPRM model using the parameters optimized for the US in WRF-Chem and showed reasonable CO_2 simulation results over Korea. Thus, to estimate CO_2 over parts of Asia, Li et al. (2020) used the modified VPRM parameters for the US, while Park et al. (2020) directly used the VPRM parameters for the US. Although Dayalu et al. (2018) used the VPRM parameters optimized for Asia to estimate CO_2 over East Asia, the VPRM parameters were optimized using past observations during 2005–2009. Therefore, to simulate recent CO_2 concentrations over East Asia, suitable VPRM parameters in WRF-Chem need to be investigated.

In addition to the biogenic emission inventory, atmospheric variables (e.g., wind) affect the simulated atmospheric CO_2 concentrations because the distribution and concentration of simulated atmospheric CO_2 are more affected by wind transport than by reactions with other chemicals in the atmosphere (Nasrallah et al. 2003). Seo and Kim (2023) showed that enhanced atmospheric variables by meteorological data assimilation have large impact in improving the accuracy of CO_2 concentration simulations in East Asia. In previous studies that simulated CO_2 concentrations using WRF-Chem, various atmospheric fields were used as the initial and boundary conditions of the model. As WRF-Chem is a regional model, initial atmospheric conditions and atmospheric boundary conditions greatly affect the simulation results and forecast error (Kim and Kim 2021). To simulate CO_2 concentrations using WRF-Chem in the US, Hu et al. (2020) used the National Center for Environmental Prediction-Department of Energy (NCEP/DOE) R2 data (Kanamitsu et al. 2002); Chen et al. (2019) and Feng et al. (2019) used the European Center for Medium-Range Weather Forecasts Interim Reanalysis (ERA-Interim; Dee et al. 2011); and Martin et al. (2019) conducted an experiment using NCEP North American Regional Reanalysis (NARR; Mesinger et al. 2006). To simulate CO_2 concentrations using WRF-Chem in China, Li et al. (2019, 2020) used NCEP/DOE R2 data, and Liu et al. (2018) used ERA-Interim data. Ballav et al. (2012) and Park et al. (2020) simulated and verified CO_2 concentrations in Tokyo and Korea using WRF-Chem, respectively, using the final analysis (FNL) of NCEP.

Although various atmospheric reanalysis fields have been used as the initial and boundary conditions in WRF-Chem for various experimental areas, no previous studies have investigated the sensitivity of simulated CO_2 concentrations with respect to atmospheric reanalysis data, especially focusing on East Asia. In addition, the sensitivity of simulated CO_2 concentrations with respect to VPRM parameters has not been investigated in East Asia. Therefore, to appropriately simulate high-resolution CO_2 concentrations in East Asia, the effects of atmospheric conditions and VPRM parameters on simulating CO_2 concentrations over East Asia need to be evaluated using WRF-Chem. Therefore, in this study, sensitivity studies using WRF-Chem were conducted to find the most appropriate experimental framework for simulating high-resolution CO_2 concentrations in East Asia.

Section 2 presents the model description and observations, Section 3 presents the results, and Section 4 provides a summary and conclusions.

2 Methods

2.1 Model

WRF-Chem is a chemical transport model based on the WRF developed by NCAR (Grell et al. 2005). The WRF-Chem version 4.1.5 was used in this study. WRF-Chem is a fully compressible non-hydrostatic model with dynamic and chemical parts integrated together in each time step (Powers et al. 2017). Because the atmospheric and chemical parts are fully coupled ("online model"), both parts are transported on the same grid, with the same physics and transport system. Because the chemical and dynamic parts affect each other, the "online" calculations can suitably simulate chemicals in the atmosphere (Grell et al. 2005).

The physical schemes used in WRF-Chem are the shortwave and longwave scheme (RRTMG (Iacono et al. 2008)), microphysics scheme (WRF Single-moment 6-class Scheme; WSM 6-class (Hong and Lim 2006)), cumulus parameterization scheme (Grell 3D Ensemble Scheme (Grell and Dévényi 2002)), planetary boundary layer physics scheme (Yonsei University (YSU) scheme (Hong et al. 2006)), surface layer scheme (Revised MM5 (Jiménez et al. 2012)), and land surface scheme (Unified Noah Land Surface model (Tewari et al. 2004)).

In WRF-Chem, CO_2 is subdivided into four components:

$$CO_2\_TOTAL = CO_2\_ANT + CO_2\_BIO + CO_2\_OCE + CO_2\_FIRE, \quad (1)$$

where CO_2_ANT is anthropogenic CO_2, CO_2_BIO is biogenic CO_2, CO_2_OCE is oceanic CO_2, and CO_2_FIRE is CO_2 due to fire. Because CO_2 is treated as an inert gas in WRF-Chem, each component does not affect the other components during integration (Zheng et al. 2019).

For CO_2 simulations in WRF-Chem, the emission input data of anthropogenic, biogenic, oceanic, and fire emissions, and background CO_2 are required. Anthropogenic and oceanic emission input data were generated from inventory data, as described in Section 2.1.1. The background CO_2 data was from that specified in CarbonTracker 2019 (CT2019). For biogenic emission, VPRM was used as described in Section 2.1.2. In this study, fire emission was not considered because the fire inventory showed few fire events during the experimental period over East Asia. The CO_2 concentrations were predicted by integrating the WRF-Chem with emission input data and atmospheric and chemical initial and boundary conditions.

2.1.1 Anthropogenic and ocean emission inventory

The Emission Database for Global Atmospheric Research (EDGAR) and the open-source data inventory for anthropogenic CO_2 (ODIAC) are widely used as anthropogenic emission inventories (Zheng et al. 2020). The EDGAR inventory generally overestimates observations around large urban area and ODIAC shows better agreement with observations (Hu et al. 2020). For this study, both EDGAR and ODIAC anthropogenic emission inventory were tested with WRF-VPRM. By using the ODIAC inventory, the simulated CO_2 concentrations become more similar to the observed CO_2 concentrations in most validation sites compared to those with EDGAR inventory, which implies that the ODIAC inventory is appropriate for CO_2 simulations in East Asia (not shown).

Therefore, the ODIAC was used as an anthropogenic CO_2 emission inventory. ODIAC is generated based on GOSAT satellite data from the National Institute for Environmental Studies (NIES) in Japan (Oda and Maksyutov 2015). Fossil fuel (i.e., anthropogenic) emissions in ODIAC are calculated using space-based nighttime light data of GOSAT, the emissions from each plant, and the latitude and longitude for each plant. ODIAC version 2019 (ODIAC 2019) was downloaded from the Center for Global Environmental Research (CGER) and NIES (http://db.cger.nies.go.jp/dataset/ODIAC/, https://doi.org/10.17595/20170411.001.). Monthly average data at a resolution of 1×1 km during 2000–2018 in GeoTIFF format in ODIAC 2019 were provided and monthly average data in March 2018 of ODIAC 2019 was used in this study. The monthly average data of the ODIAC emission inventory have been used as an anthropogenic emission inventory in multiple studies (Li et al. 2019, 2020; Hu et al. 2020).

The ocean CO_2 map from the Japan Meteorological Agency (JMA), with a spatial resolution of $1° \times 1°$ (Iida et al. 2021; Takatani et al. 2014), was used as the oceanic CO_2 emission inventory. The ocean CO_2 map provides the air–sea CO_2 flux, pH, carbon dioxide partial pressure (pCO_2), dissolved inorganic carbon (DIC) concentration, and total alkalinity (TA). Among these, pCO_2 is calculated from sea surface temperature (SST), chlorophyll-a, and salinity observations from a satellite (Takatani et al. 2014).

2.1.2 Vegetation Photosynthesis and Respiration Model (VPRM)

VPRM (Mahadevan et al. 2008) is a model for calculating biogenic CO_2 in WRF-Chem, and was combined with WRF-Chem starting from version 3.1.1 (Xiao et al. 2004; Ahmadov et al. 2007). Before conducting VPRM, a pretreatment process called the VPRM preprocessor needs to be performed. MODerate resolution Imaging Spectroradiometer (MODIS) satellite observations were used in the VPRM preprocessor. The MODIS is operated on two spacecraft, Terra and Aqua. In this study, the MOD09A1 version 6 of Terra was used. The enhanced vegetation index (EVI) and the land surface water index (LSWI) were calculated in the VPRM preprocessor using the surface reflectance values of MOD09A1 for each land use type of the synergetic land cover product (SYNMAP) proposed by Jung et al. (2006).

The VPRM was calculated simultaneously with model integration. In VPRM, the sum of GEE and R are calculated for each land use type using EVI and LSWI from the VPRM preprocessor and 2 m temperature and downward shortwave radiation from WRF. The calculation formula is as follows (Mahadevan et al. 2008):

$$GEE = \lambda \times T_{scale} \times P_{scale} \times W_{scale} \times EVI \times \frac{1}{\left(1 + \frac{PAR}{PAR_0}\right)} \times PAR \tag{2}$$

$$R = \alpha \times T + \beta \tag{3}$$

where PAR is photosynthetically activate radiation and calculated using downward shortwave radiation from WRF; α, β, λ, and PAR_0 are empirical parameters for each land use type; T is 2 m temperature from WRF; T_{scale} denotes the relationship between photosynthesis and temperature, P_{scale} denotes the effect of leaf expansion, and W_{scale} denotes canopy moisture calculated from LSWI of the MODIS satellites, which are dimensionless variables with values between 0 and 1 (Hilton et al. 2013) and calculated using the following equations.

$$T_{scale} = \frac{\left(T - T_{min}\right)\left(T - T_{max}\right)}{\left(T - T_{min}\right)\left(T - T_{max}\right) - \left(T - T_{opt}\right)^2} \tag{4}$$

$$P_{scale} = \frac{1 + LSWI}{2} \tag{5}$$

$$W_{scale} = \frac{1 + LSWI}{1 + LSWI_{max}} \tag{6}$$

where T_{max}, T_{min}, and T_{opt} represent the maximum, minimum, and optimum temperatures during photosynthesis, respectively, and are provided as tables for each land use type in VPRM, and $LSWI_{max}$ denotes the maximum LSWI in the growing season.

In VPRM simulations of biogenic CO_2 in WRF-Chem, α, β, λ, and PAR_0 should be optimized for the experimental region (Hilton et al. 2013). In this study, three tables previously used for East Asia were used to investigate the VPRM parameter table that is the most appropriate over East Asia. The three tables are the US table, Li table (used by Li et al. 2020), and Dayalu table (used by Dayalu et al. 2018) (Table 1).

2.1.3 Initial and boundary conditions of WRF-Chem

As WRF-Chem is a regional model that combines meteorology and chemistry, the chemical initial and boundary conditions and the atmospheric initial and boundary conditions are required to run the WRF-Chem. Since the atmospheric CO_2 concentration is primarily affected by the transport of CO_2 rather than chemical reactions (Nasrallah et al. 2003), only chemical initial and boundary conditions for CO_2 were used as the chemical initial and boundary conditions.

In accordance with previous studies (Li et al. 2019; Li et al. 2020; Liu et al. 2018; Park et al. 2020), CT2019 data from the ESRL of NOAA (Jacobson et al. 2020) were used as the chemical initial and boundary conditions for CO_2. The global CO_2 concentrations of CT2019 are provided at a spatial resolution of 3°×2°. As in WRF-Chem, CO_2 in CT2019 is subdivided into four components: CO_2_ANT, CO_2_BIO, CO_2_OCE, and CO_2_FIRE. As in WRF-Chem, the fire emission in CT2019 was not considered.

The fifth generation atmospheric reanalysis of the European Centre for Medium-range Weather Forecasts (ECMWF; ERA5) (Hersbach et al. 2018) and FNL of NCEP (NCEP/NOAA 2000) were used as atmospheric initial and boundary conditions.

2.2 Experimental design

To investigate the most appropriate atmospheric initial and boundary conditions and VPRM tables for simulating CO_2 over East Asia, several experiments were conducted for the one-month period of March 2018.

Table 2 shows the configuration of WRF-Chem used in this study. The horizontal resolution of WRF-Chem was set to 9 km with 393×336 grid points over the experimental region, as shown in Fig. 1. The model's vertical layers were 51 vertical layers with the top of the model as 50 hPa.

Table 1 VPRM parameter values for different vegetation types in each VPRM table

		Trees evergreen	Trees deciduous	Trees mixed	Trees and shrubs	Trees and grasses	Trees and crops	Grasses
US table	PAR_0	261	324	206	363	682	757	157
	λ	0.2492	0.1729	0.2555	0.08736	0.1141	0.1533	0.13335
	α	0.3301	0.3258	0.3422	0.0239	0.0049	0.268	0.0269
	β	0	0	0	0	0	0	0
Li table	PAR_0	745.306	514.13	419.5	590.7	600	1074.9	717.1
	λ	0.13	0.1	0.1	0.18	0.18	0.085	0.115
	α	0.1247	0.092	0.2	0.0634	0.2	0.13	0.0515
	β	0.2496	0.843	0.27248	0.2684	0.3376	0.542	-0.0986
Dayalu table	PAR_0	786	324	639	1405	682	1768.3	464
	λ	0.0903	0.1729	0.129	0.104	0.1141	0.119	0.0451
	α	0.128	0.3258	0.267	0.162	0.0049	0.078	0.0306
	β	-0.464	0	-0.291	-0.71	0	0.44971	0.0919

Table 2 Configuration of WRF-Chem simulation

Experimental period		2018.02.22 – 2018.03.31 (Spin-up: 7 days from 22 to 28 February 2018)
Resolution	Horizontal	9 km × 9 km with 393 × 336 grid points
	Vertical	51 layers (top: 50 hPa)
	Time step	30 s
Initial and lateral boundary conditions	Chemical (CO_2)	CT2019
	Meteorological	FNL, ERA5
Emission Inventory	Anthropogenic	ODIAC 2019
	Biosphere	VPRM model
	Ocean	JMA
Physics schemes	Shortwave radiation	RRTMG
	Longwave radiation	RRTMG
	Microphysics	WSM 6-class
	Cumulus	Grell 3D Ensemble
	PBL	YSU
	Surface Layer	Revised MM5
	Land Surface	Noah

Figure 2 shows the schematic diagram to simulate CO_2 using WRF_Chem. From 1 March 2018, a 30-h prediction of WRF-Chem was conducted every 18 UTC, and the previous 24 h CO_2 prediction field was used as the initial condition for the next run as in Pillai et al. (2011) and Zhao et al. (2019). This was to simulate long-distance transport by allowing CO_2 transported in the previous run to be reflected in the next run (Ballav et al. 2012; Liu et al. 2018; Li et al. 2019, 2020). The emission inventory, atmospheric initial and boundary conditions (i.e., FNL and ERA5), and chemical boundary conditions (i.e., CT2019) were updated every 18 UTC. To run the WRF-Chem for the one-month period of March 2018, 7 days of model spin up was performed from February 22 to 28, 2018, as Ballav et al. (2012) and Ballav et al. (2020) have used 5 days of model spin up to simulate CO_2 concentrations for 1–2 years over Asia. The validation used only 24-h forecasts from 6 to 30 h.

Table 3 shows the experimental names depending on the atmospheric conditions and the VPRM table used.

2.3 Validation

Validation was performed for the 24 h forecast field from 6 to 30 h forecasts, to avoid possible discontinuities caused by initial and boundary condition updates.

For validation, the bias and root mean square error (RMSE) were used and calculated as:

$$Bias = R_i - O_i \tag{7}$$

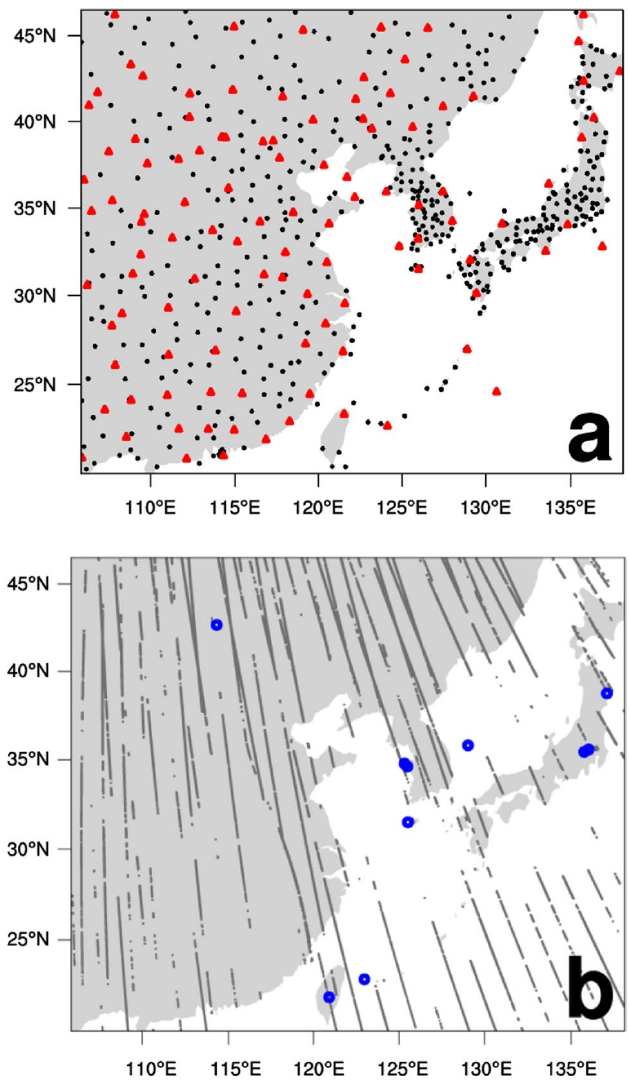

Fig. 1 **a** Meteorological observation sites (SYNOP: black dot, SONDE: red triangle) and **b** CO_2 observation sites (surface CO_2 observation sites: blue dot, OCO-2 XCO_2 observation sites: grey dot) in the model domain

$$RMSE = [\frac{1}{n}\sum_{i=1}^{n}(R_i - O_i)^2]^{1/2} \tag{8}$$

where R is the model simulation value, O is the observed value, and n is the number of observations.

2.3.1 Meteorological observations for validation

For the atmospheric field, the NCEP PrepBUFR conventional observations were used to validate the surface and upper-air simulation results. For surface observations, the wind speed and direction of land surface synoptic weather observations (SYNOP) were used every 6 h (00, 06, 12, and 18 UTC). For upper-air observations, upper-air wind profiles from radiosonde (SONDE) observation data at 925, 700, 500, 300, and 200 hPa were used every 12 h (00, 12 UTC). Figure 1a shows the locations of the SYNOP and SONDE observations used in this study.

2.3.2 CO_2 observations and model output for validation

Various CO_2 observations were used to examine whether the CO_2 concentrations were accurately simulated in WRF-Chem. Table 4 provides information on surface CO_2 observation sites used for validation. CO_2 observation data for Anmyeon-do (AMY, Republic of Korea), Mt. Dodaira (DDR, Japan), Kisai (KIS, Japan), Lulin (LLN, Taiwan, Province of China), Ryori (RYO, Japan), Tae-ahn Peninsula (TAP, Republic of Korea), Ulaan Uul (UUM, Mongolia), and Yonagunijima (YON, Japan) are provided by the World Data Centre for Greenhouse Gases (WDCGG, https://ds.data.jma.go.jp/wdcgg). These data are observed by NOAA ESRL, Center for Environmental Science in Saitama (SAIPF, Japan), JMA, and Korea Meteorological Administration (KMA; Republic of Korea). The Gosan (GSN, Republic of Korea) and Ulleung-do (UL, Republic of Korea) observations are provided by KMA (https://data.

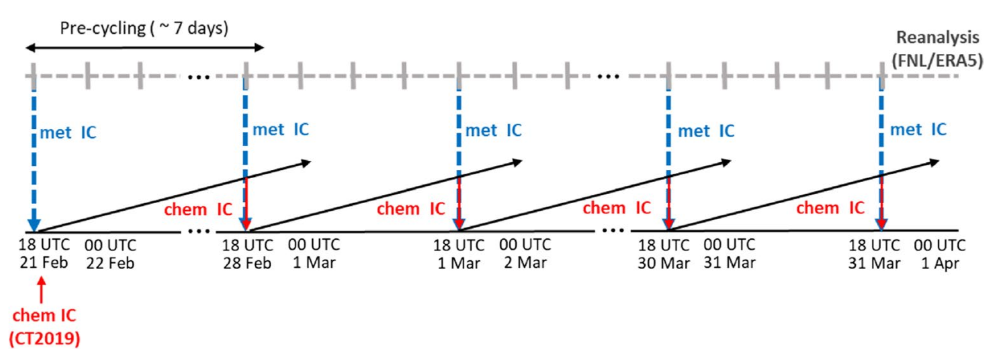

Fig. 2 The schematic diagram of the CO_2 simulation using WRF-Chem

Table 3 Experiment names depending on meteorological initial and boundary conditions and VPRM tables

Experimental name	Meteorological initial and lateral boundary conditions	VPRM table
FNL_US	FNL	US table
FNL_ Li	FNL	Li table
FNL_Da	FNL	Dayalu table
ERA_US	ERA5	US table
ERA_ Li	ERA5	Li table
ERA_Da	ERA5	Dayalu table

kma.go.kr/data/gaw/selectGHGsRltmList.do?pgmNo=587). The observation data for AMY, DDR, KIS, RYO, and YON are at 1 h intervals, GSN and UL data are at 1 day intervals, and LLN, TAP, and UUM provide data discontinuously.

Satellite-based XCO_2 observations were used to compensate for the lack of surface CO_2 observations over East Asia. OCO-2 is the National Aeronautics and Space Administration (NASA)'s first Earth remote sensing satellite for atmospheric CO_2 observations, launched after GOSAT. OCO-2 provides a space-based global measurement for the absorption and emission of local CO_2 and carries out observations at 13:30 LST along a solar synchronous orbit. The OCO-2 observation data used were ACOS L2 Lite Output Filtered with oco2-lite_file_prefilter_b9 converted from Level 1 radiance to Level 2 data using the ACOS retrieval algorithm (O'Dell et al. 2012), produced by the Jet Propulsion Laboratory (JPL) (https://co2.jpl.nasa.gov/download/?dataset=OCO2LtCO2v9&product=LITE). The data quality of the OCO-2 observations can be checked by the values of xco2_quality_flag and warn_level as described in the OCO-2 Data Product User's Guide (Osterman et al. 2018). The xco2_quality_flag value is 0 or 1, where 0 means "good" and 1 means "bad". In this study, OCO-2 data with '0' xco2_quality_flag value were used for validation.

In WRF-Chem, CO_2 concentrations are simulated at each pressure level, while OCO-2 observes the column-averaged CO_2 mole fraction (XCO_2). Because the data types of the simulated CO_2 and satellite observed XCO_2 are different, they need to be converted into the same data type for comparison. Thus, CO_2 concentrations simulated at each pressure level in WRF-Chem were converted to XCO_2 concentrations. First, the simulated CO_2 concentrations in WRF-Chem were interpolated to the latitude and longitude of OCO-2 data. Then, the XCO_2 concentrations of WRF-Chem were calculated as in Connor et al. (2008) and O'Dell et al. (2012):

$$XCO_2^{model} = XCO_{2a} + \sum_i w_i^T A_i \left(CO_2^{interp} - CO_{2a} \right)_i \tag{9}$$

where XCO_{2a} is a priori XCO_2, w_i^T is the pressure weighting function, A_i is the column averaging kernel, CO_2^{interp} is the interpolated simulated CO_2 concentrations of WRF-Chem, and CO_{2a} is a priori CO_2.

Figure 1b shows the locations of the surface CO_2 and satellite XCO_2 observations used in this study. In addition to surface CO_2 and satellite XCO_2 observations, the CarbonTracker output (CT2019) was used to validate the reliability of the simulated CO_2 concentrations.

3 Results

3.1 Distribution of surface biogenic CO_2 concentrations

Figure 3a shows the average surface biogenic CO_2 concentrations simulated in the six experiments, and Fig. 3b shows the surface biogenic CO_2 concentrations in CT2019. In the surface CO_2 concentrations averaged for six experiments (Fig. 3a), the CO_2 absorption by vegetation is

Table 4 Information on surface CO_2 observation sites

Site	Latitude (°)	Longitude (°)	Height (m)	Laboratory	Observation time interval
AMY	36.54	126.33	42	NOAA/ESRL	Hourly
DDR	36.00	139.20	840	SAIPF	Hourly
KIS	36.08	139.55	13	SAIPF	Hourly
LLN	23.47	120.87	2862	NOAA/ESRL	Event
RYO	39.03	141.82	260	JMA	Hourly
TAP	36.73	126.13	20	NOAA/ESRL	Event
UUM	44.45	111.10	992	NOAA/ESRL	Event
YON	24.47	123.01	30	JMA	Hourly
GSN	33.15	126.12	72	KMA	Daily
UL	37.48	130.90	220.9	KMA	Daily

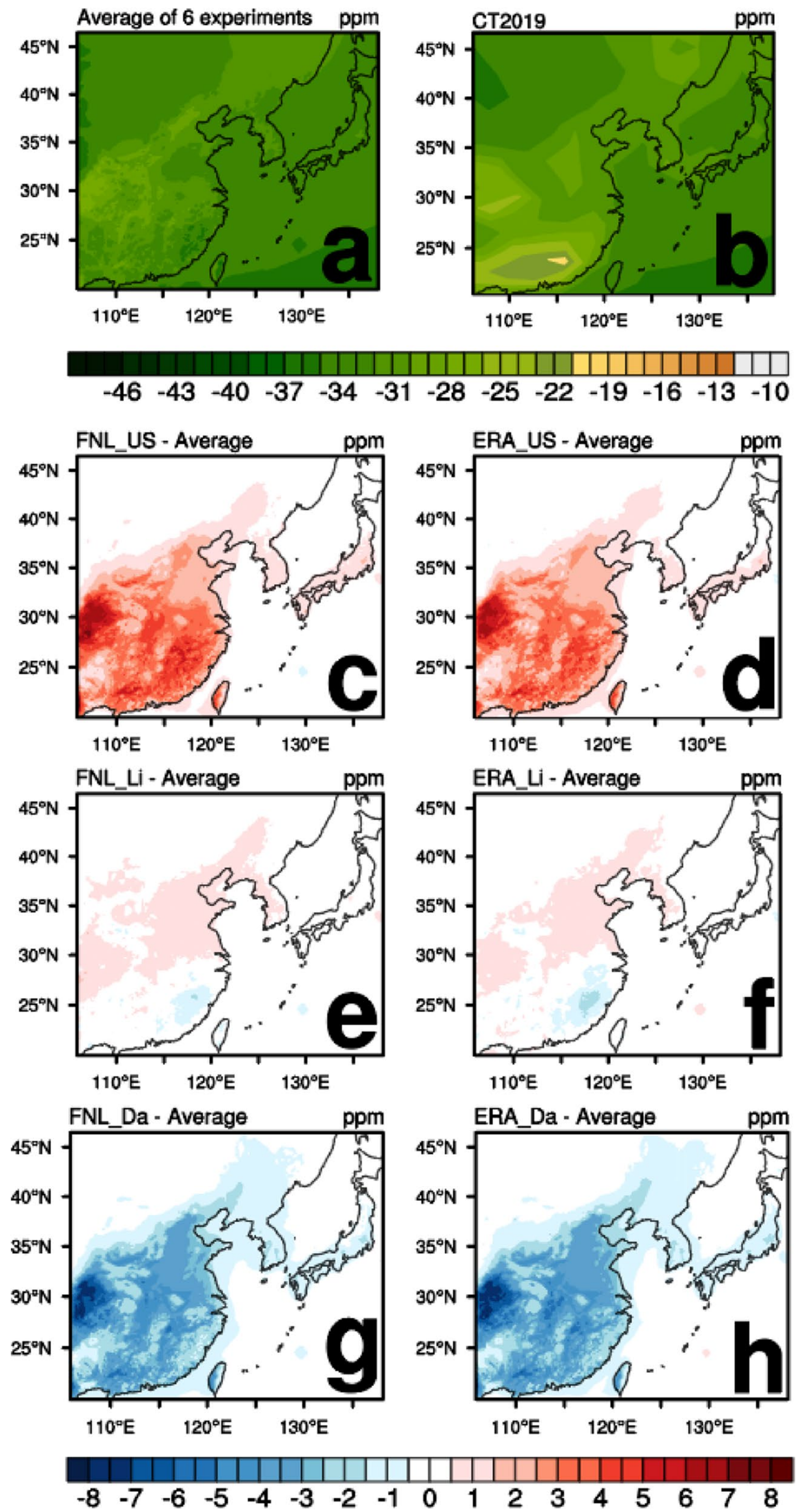

Fig. 3 Distribution of **a** average surface biogenic CO_2 concentration (ppm) simulated in six experiments and **b** surface biogenic CO_2 concentration (ppm) in CT2019. Anomaly distributions for average surface biogenic CO_2 concentration (ppm), simulated in **c** FNL_US, **d** ERA_US, **e** FNL_Li, **f** ERA_Li, **g** FNL_Da, and **h** ERA_Da from the average of six experiments shown in (**a**)

weaker over central China and the Korean Peninsula than that in other regions. These regional patterns of the averaged simulation results are similar to those of the biogenic CO_2 concentrations in CT2019 in Fig. 3b. Because the horizontal resolution of the experiments was denser than that in CT2019, more detailed distributions were simulated in the experiments using WRF-Chem. However, the amplitude of biogenic CO_2 absorption in the averaged simulation results in WRF-Chem is greater than that in CT2019 (compare Fig. 3a and b). This difference in biogenic CO_2 may be due to different model framework between WRF-Chem and CT2019.

Figures 3c–h show the difference between the surface biogenic CO_2 concentrations of each experiment and the average biogenic CO_2 concentrations over six experiments. FNL_US and ERA_US show very similar distributions and amount of biogenic CO_2 concentrations (Fig. 3c and d), indicating that the difference in atmospheric initial and boundary conditions for WRF-Chem simulations did not seem to significantly affect the simulated biogenic CO_2 concentrations. Compared to the average biogenic CO_2 concentrations, FNL_US (Fig. 3c) and ERA_US (Fig. 3d) show lower biogenic CO_2 absorption over central China and the Korean Peninsula. This underestimated biogenic CO_2 absorption in both FNL_US and ERA_US compared to the average biogenic CO_2 absorption results in greater differences in Fig. 3c and d.

FNL_Li and ERA_Li show very similar distributions and amount of biogenic CO_2 concentrations (Fig. 3e and f). Compared to the average biogenic CO_2 concentrations, FNL_Li (Fig. 3e) and ERA_Li (Fig. 3f) show lower biogenic CO_2 absorption over central China and the Korean Peninsula and greater biogenic CO_2 absorption in southern China. However, the magnitude of the differences between the simulated biogenic CO_2 concentrations (FNL_Li and ERA_Li) and the average is small.

FNL_Da and ERA_Da also show similar distributions of biogenic CO_2 concentrations (Fig. 3g and h). Compared to the average biogenic CO_2 concentrations, FNL_Da (Fig. 3g) and ERA_Da (Fig. 3h) show greater biogenic CO_2 absorption over central China and the Korean Peninsula. This overestimated biogenic CO_2 absorption in both FNL_Da and ERA_Da compared to the average biogenic CO_2 absorption results in greater differences (Fig. 3g and h).

In contrast to the similar distribution and magnitude of biogenic CO_2 concentrations between the experiments using different atmospheric initial and boundary conditions and the same VPRM table, there were substantial differences between the experiments using the same atmospheric initial and boundary conditions and different VPRM tables. Therefore, the simulated surface biogenic CO_2 concentrations were more sensitive to differences in the VPRM tables than those in the atmospheric initial and boundary conditions. In terms of region, the differences in biogenic CO_2 concentrations in the experiments were the greatest over central China and the Korean peninsula.

The distributions of the simulated total CO_2 concentrations (not shown), which are the sum of the biogenic, anthropogenic, oceanic, and background CO_2 concentrations, showed similar distributions as in Fig. 3.

3.2 Validation with observations

As the simulated CO_2 concentrations may be affected by the simulated transport, the simulated wind speed and direction were validated against the observed wind speed and direction. In addition, the simulated CO_2 concentrations of each experiment were compared with the observed CO_2 concentrations to validate whether the simulation results were appropriate and to investigate the experiment that led to the most accurate simulation results.

3.2.1 Validation of wind speed and direction

In WRF-Chem, the atmospheric and chemical fields interact with each other. According to Baklanov et al. (2014), in WRF-Chem, various atmospheric variables such as temperature, precipitation, wind direction, and wind speed can affect the chemical species. In addition, the physical characteristics of aerosols and the concentrations of radiatively active gases can affect atmospheric variables. However, in this study, only CO_2 was simulated without considering the reaction with aerosols in the atmosphere. Therefore, there was no change in the atmospheric field with changes in the CO_2 concentration.

Among the six experiments in Table 3, the experiments with the same atmospheric initial and boundary conditions simulated the same atmospheric fields. This implies that the atmospheric fields of FNL_US, FNL_Li, and FNL_Da were simulated identically. Thus, when verifying the atmospheric field, the six experiments can be divided into two groups: experiments using FNL (FNL_exp) and experiments using ERA5 (ERA_exp).

Figure 4 shows the time series of bias and RMSE for each experimental result (i.e., FNL_exp and ERA_exp) with respect to surface SYNOP observations for wind speed and direction. The bias and RMSE for each experiment are summarized in Table 5. For both FNL_exp and ERA_exp, the biases of the surface wind speed show high fluctuations centered around 0 (Fig. 4a), leading to small bias values (0.05 and 0.01 m s^{-1} in FNL_exp and ERA_exp, respectively) for both experiments (Table 5) despite high fluctuations. The RMSEs of the surface wind speed in both experiments showed high fluctuations (Fig. 4b) with an approximate value of 3.2 m s^{-1} (Table 5). In contrast to wind speed, the biases of the surface wind direction were mostly positive (Fig. 4c), implying that the surface wind direction in both experiments was overestimated compared to the observation values. The bias for FNL_exp (ERA_exp) was 22.84° (24.05°) (Table 5). The RMSEs of the surface wind direction in both experiments showed large values (Fig. 4d) with 82.81° for FNL_exp and 84.21° for ERA_exp

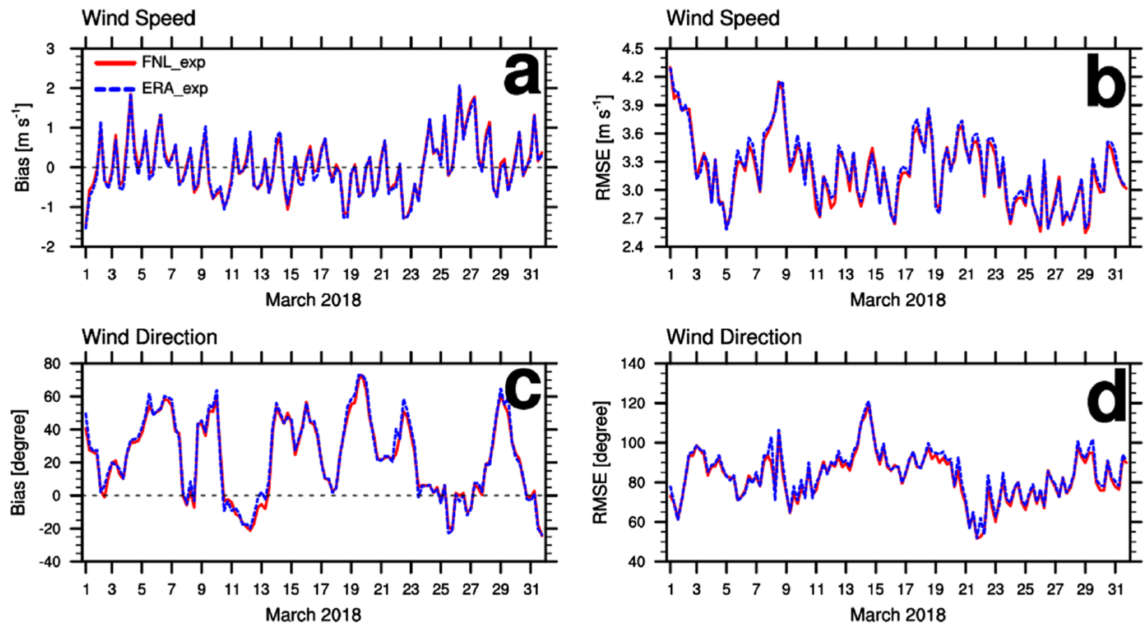

Fig. 4 Time series of **a** bias and **b** RMSE of simulated 10 m wind speed (m s^{-1}) with respect to the observed 10 m wind speed at SYNOP sites during March 2018. Time series of **c** bias and **d** RMSE of simulated 10 m wind direction (°) with respect to the observed 10 m wind direction at SYNOP sites in March 2018. FNL_exp (ERA_exp) is denoted by red (blue) line

(Table 5). Compared to the surface wind speed with smaller bias and RMSE, the surface wind direction showed a large bias and RMSE compared to the observed values for both experiments. Although the difference between FNL_exp and ERA_exp was small for both surface wind speed and direction, FNL_exp showed a slightly smaller bias and RMSE than ERA_exp.

Figure 5 shows the time series of wind speed, bias, and RMSE for each experimental result (i.e., FNL_exp and ERA_exp) with respect to the upper-air SONDE observations at each pressure level. The bias and RMSE for each experiment are summarized in Table 6. For both FNL_exp and ERA_exp, the wind speed and bias increased as go up into the upper atmosphere (Fig. 5a–c). The average biases of wind speed below 700 hPa (at 500 hPa) were 0.20 and 0.22 m s^{-1} (-0.63 and -0.71 m s^{-1}) in FNL_exp and ERA_exp, respectively (Table 6). In contrast to the negative biases in other layers, the biases of the wind speed at 925 hPa were positive in both experiments (Fig. 5c and Table 6), which implies an overestimation of the wind speed at 925 hPa in both experiments. As the wind speed increased in the upper atmosphere, the biases in the upper atmosphere also increased (Fig. 5d–f). Similar to the bias, for both experiments, the RMSE increased as go up into the upper atmosphere (Fig. 5g–i). The average RMSEs of wind speed below 700 hPa (at 500 hPa) are 4.00 and 4.04 m s^{-1} (6.45 and 6.50 m s^{-1}) in FNL_exp and ERA_exp, respectively (Table 6).

Table 5 Bias and RMSE of the simulated 10 m wind speed and direction for FNL_exp and ERA_exp with respect to the observed 10 m wind speed and direction at SYNOP sites

	Wind speed [m s^{-1}]		Wind direction [°]	
	FNL_exp	ERA_exp	FNL_exp	ERA_exp
Bias	0.045	0.011	22.839	24.054
RMSE	3.202	3.230	82.807	84.208

Figure 6 shows the time series of wind direction, bias, and RMSE for each experimental result (i.e., FNL_exp and ERA_exp) with respect to the upper-air SONDE observations for wind direction at each pressure level. The bias and RMSE for each experiment are summarized in Table 6. For both FNL_exp and ERA_exp, the wind direction was approximately less than 240° in the lower atmosphere at 925 hPa and greater than 240° above 700 hPa (Fig. 6a–c), implying that the wind is veering towards the east in the lower atmosphere. In contrast to the wind direction, the fluctuations of wind direction and bias decreased as go up into the upper atmosphere (Fig. 6a–c). The high fluctuation in wind direction in the lower atmosphere is due to the complex topography. The average biases of the wind direction below 700 hPa (at 500 hPa) were 8.93° and 7.99° (5.20° and 4.58°) in FNL_exp and ERA_exp, respectively (Table 6). For both experiments, the wind direction was mostly overestimated at all levels (Fig. 6d–f and Table 6). Similar to the bias, for both experiments, the RMSE increased as go down into the lower atmosphere (Fig. 6g–i). The average

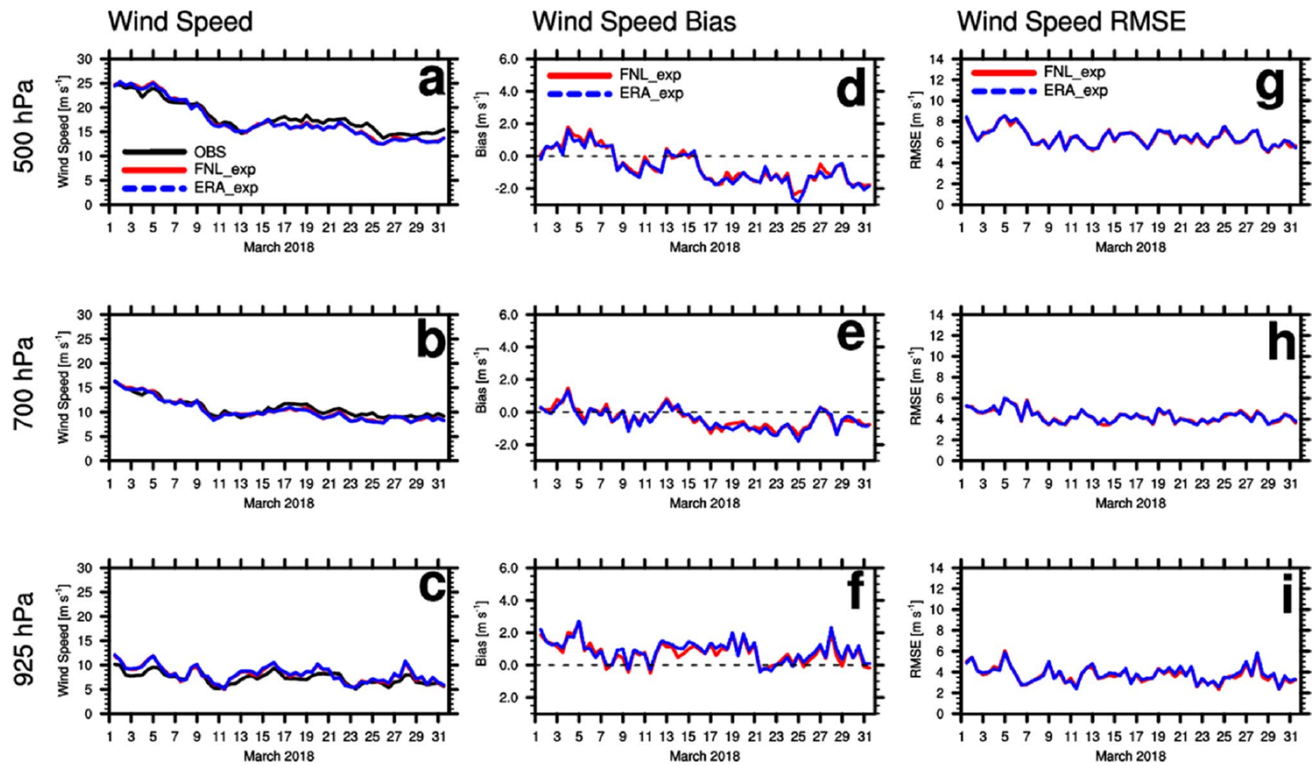

Fig. 5 Time series of **a–c** simulated wind speed (m s^{-1}), **d–f** bias (m s^{-1}) of simulated wind speed, and **g–i** RMSE (m s^{-1}) of simulated wind speed with respect to the observed wind speed at SONDE sites at each pressure level in March 2018. FNL_exp (ERA_exp) is denoted by red (blue) line

Table 6 Bias and RMSE of the simulated wind speed and direction for FNL_exp and ERA_exp with respect to the observed wind speed and direction at SONDE sites at each pressure level

		Wind speed [m s^{-1}]		Wind direction [°]	
		FNL_exp	ERA_exp	FNL_exp	ERA_exp
Bias	500 hPa	-0.630	-0.712	5.203	4.577
	700 hPa	-0.381	-0.451	6.073	4.833
	925 hPa	0.778	0.882	11.777	11.156
	Average	-0.078	-0.093	7.684	6.855
RMSE	500 hPa	6.450	6.499	32.117	32.251
	700 hPa	4.272	4.284	47.145	46.923
	925 hPa	3.720	3.789	58.877	59.382
	Average	4.814	4.857	46.046	46.185

RMSEs of the wind direction below 700 hPa (at 500 hPa) were 53.01° and 53.15° (32.12° and 32.25°) in FNL_exp and ERA_exp, respectively (Table 6). In both wind direction and wind speed, the difference between FNL_exp and ERA_exp was not large, as for the surface wind field validation. However, the mean RMSE of FNL_exp was smaller in the lower atmosphere (below 700 hPa) as well as in the upper atmosphere (at 500 hPa) (Table 6). In other words, the wind field of the entire atmosphere was slightly better simulated by FNL_exp.

Throughout the atmosphere from 925 to 500 hPa, the average RMSE of wind speed in FNL_exp was 4.81 m s^{-1} and that in ERA_exp was 4.86 m s^{-1}. For the wind direction, the average RMSE of FNL_exp was 46.05° and that of ERA_exp was 46.19°. Therefore, based on the surface and pressure level validations, FNL_exp showed slightly better results for wind forecasts than ERA_exp in East Asia.

3.2.2 Validation of simulated surface CO_2 concentrations with observed surface CO_2 concentrations

The simulated surface CO_2 concentrations in the six experiments were validated with respect to the observed surface CO_2 concentrations. In addition to the observed surface CO_2 concentrations, a comparison with surface CO_2 concentrations simulated in CT2019 was conducted to validate the reliability of the surface CO_2 concentrations simulated in this study.

Figure 7 shows the time series of the simulated surface CO_2 concentrations in this study and in CT2019 for each surface CO_2 observation site during March 2018. The simulated surface CO_2 concentrations were mostly similar to the

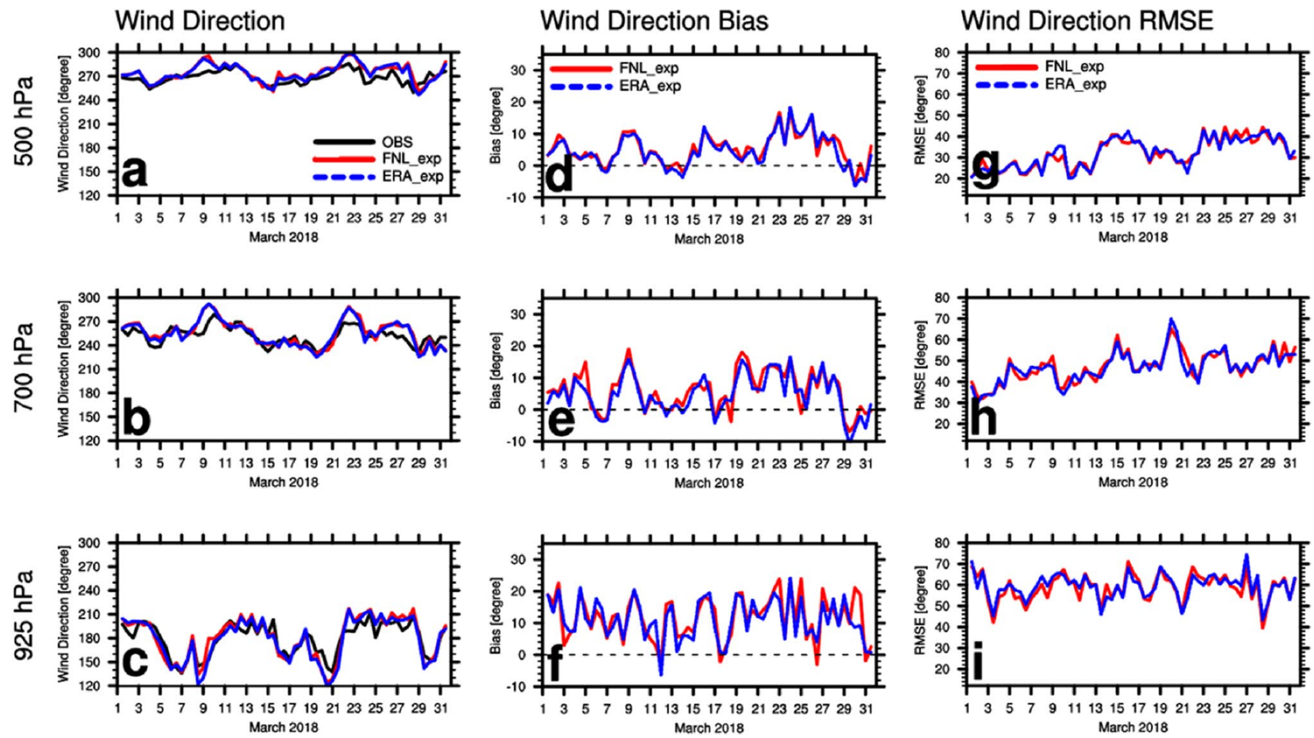

Fig. 6 Time series of **a**–**c** simulated wind direction (°), **d**–**f** bias (°) of simulated wind direction, and **g**–**i** RMSE (°) of simulated wind direction with respect to the observed wind direction at SONDE sites at each pressure level in March 2018. FNL_exp (ERA_exp) is denoted by red (blue) line

observed surface CO_2 concentrations at DDR, KIS, RYO, YON, GSN, and UL (Fig. 7a, b, c, d, f, and g). Except for GSN, the simulated surface CO_2 concentrations averaged over the six experiments were more similar to the observed surface CO_2 concentrations than those in CT2019. In the case of UUM, TAP, and LLN, surface CO_2 concentrations are rarely observed (i.e., approximately once a week), which makes comparisons of simulated surface CO_2 concentrations difficult. Nevertheless, the simulated surface CO_2 concentrations were mostly similar to the observations at UUM, TAP, and LLN (Fig. 7h, i, and j), indicating the reliability of the simulated surface CO_2 concentrations. Compared to the six experiments, CT2019 overestimated the observations at every site (Fig. 7). This overestimation is caused by the anthropogenic emission inventory used in CT2019, which are both Miller emission dataset based on EDGAR v4.2 (European Commission 2011) and ODIAC 2018 (Oda and Maksyutov 2015; Oda et al. 2018). As mentioned in Section 2.1.1, EDGAR anthropogenic emission inventory generally overestimates the observations around local anthropogenic sources (e.g., urban areas).

Figure 8 shows the biases and RMSEs for each experimental result with respect to the observed surface CO_2 concentrations at each site. The bias and RMSE for each experiment at each site are shown in Table 7. For rarely observed sites (i.e., UUM, TAP, and LLN), bias and RMSE may not be accurately calculated. Therefore, bias and RMSE were calculated for only seven sites, excluding UUM, TAP, and LLN. The biases were mostly negative except for some experiments at the KIS and YON sites (Fig. 8a and Table 7), which implies that the simulated surface CO_2 concentrations mostly underestimated the observed surface CO_2 concentrations. Except for AMY with a bias of − 4.71 ppm, the biases at other sites were smaller than 3 ppm (Fig. 8a and Table 7). This is because the simulated CO_2 concentrations at AMY were more underestimated than those at other sites, as shown in Figs. 7e and 8a. Among the observation sites, the bias was the smallest at YON (0.01 ppm averaged over six experiments) (Table 7). Among six experiments, FNL_US showed the lowest bias of − 1.18 ppm, followed by ERA_US (− 1.26 ppm) and FNL_Li (− 1.49 ppm) (Table 7). The average biases of all six experiments were less than the bias of CT2019 (Table 7). The RMSEs of KIS, RYO, YON, GSN, and UL were lower than 5 ppm, while the RMSEs of DDR and AMY were greater than 5 ppm (Fig. 8b and Table 7). Among the observation sites, the RMSE at YON was the smallest (1.62 ppm averaged over six experiments) and was much smaller than that of CT2019 (Table 7). On average, the RMSEs of the six experiments were smaller than the RMSE of CT2019 (Table 7). This implies that the surface CO_2 concentrations can be simulated more appropriately using high-resolution WRF-Chem compared to a low-resolution global

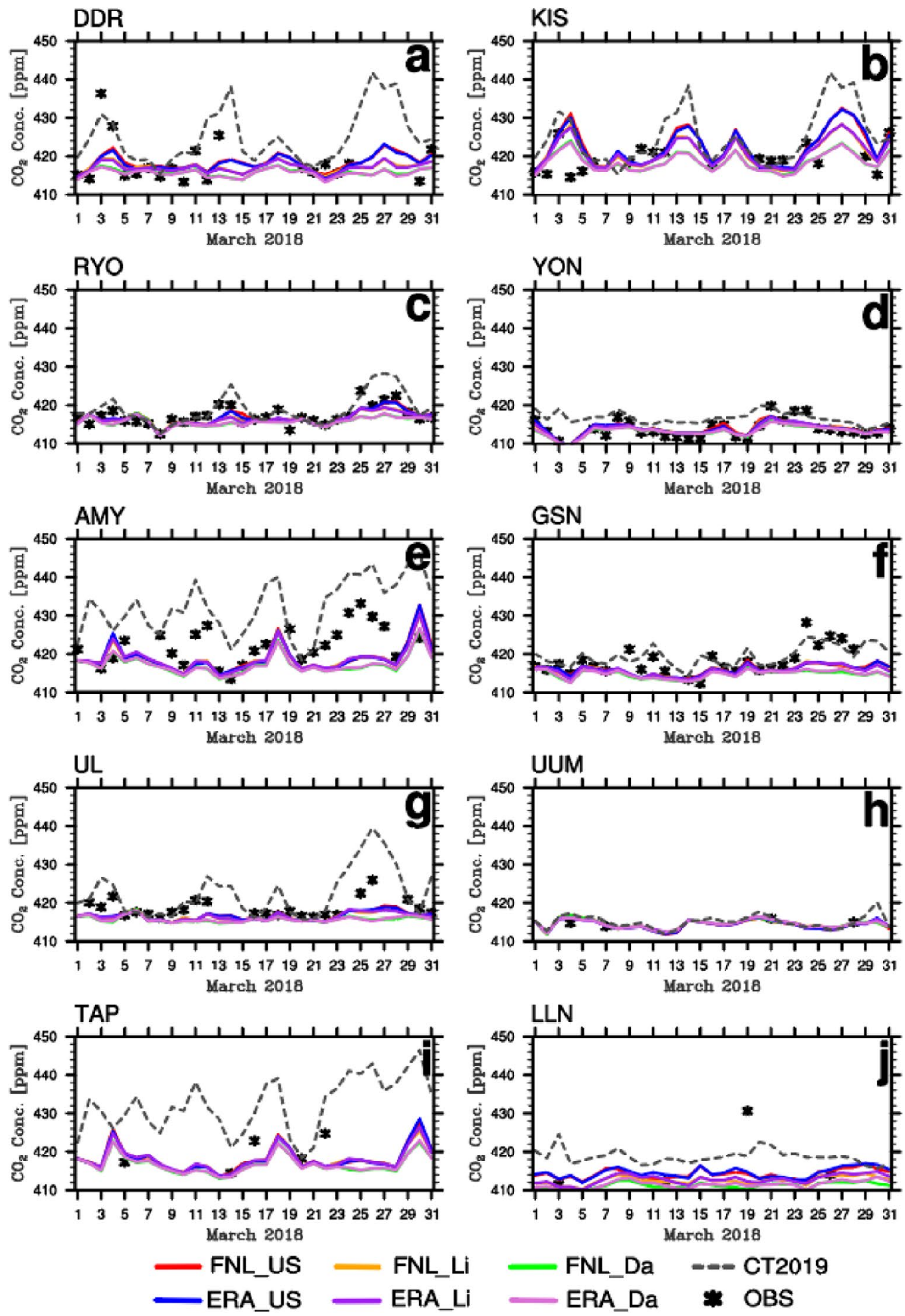

Fig. 7 Time series of simulated and observed surface CO_2 concentrations (ppm) for each surface CO_2 observation site in March 2018 (FNL_US: red solid, FNL_Li: orange solid, FNL_Da: green solid, ERA_US: blue solid, ERA_Li: purple solid, ERA_Da: light purple solid, CT2019: grey dashed, surface CO_2 observation: black star)

model (e.g., CarbonTracker). Among the six experiments, on average, ERA_Li showed the lowest RMSE (3.68 ppm), followed by FNL_Li (3.71 ppm) (Table 7).

Overall, owing to the comparable surface wind fields, FNL_exp showed a similar bias and RMSE for surface CO_2 concentrations compared to ERA_exp. For the VPRM tables, the experiments with the Li tables showed smaller biases and RMSEs compared to those with other tables. ERA_Li and FNL_Li showed smaller biases and RMSEs than the other four experiments and much smaller biases and RMSEs than CT2019. Even for the highly underestimated site as AMY, the biases and RMSEs of FNL_Li were the smallest among the six experiments and CT2019. Therefore, ERA_Li and FNL_Li showed the most similar simulated

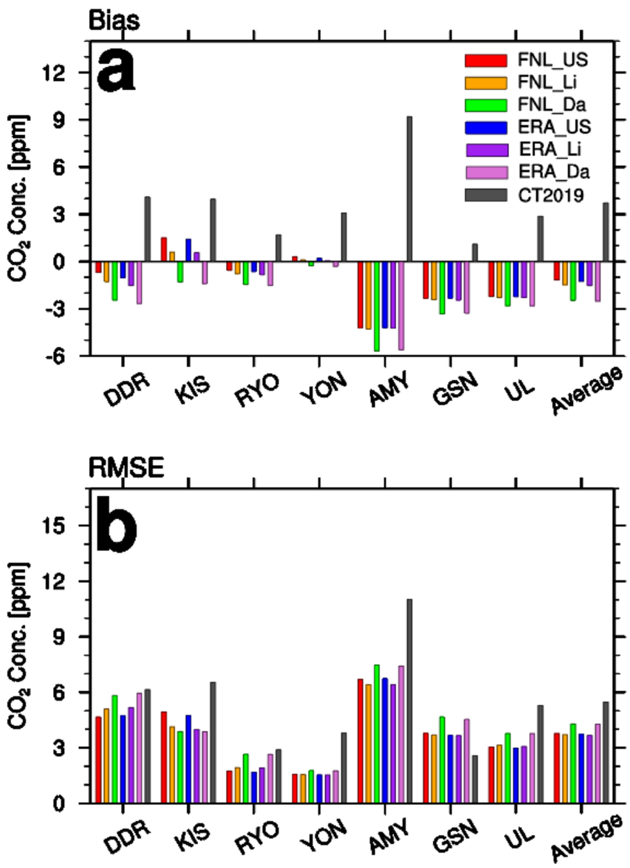

Fig. 8 **a** Bias (ppm) and **b** RMSE (ppm) of simulated surface CO_2 concentrations for each experiment and CT2019 with respect to the observed surface CO_2 concentrations at surface CO_2 observation sites (FNL_US: red, FNL_Li: orange, FNL_Da: green, ERA_US: blue, ERA_Li: purple, ERA_Da: light purple, CT2019: grey)

surface CO_2 concentrations to the observed surface CO_2 concentrations among the six experiments.

3.2.3 Validation of simulated XCO_2 concentrations with observed OCO-2 XCO_2 concentrations

The distributions of surface CO_2 observation sites are limited, and there are few surface CO_2 observation sites available in central China. For a more reliable validation, it is necessary to validate the simulated surface CO_2 observations in the regions with few surface CO_2 observation sites. Therefore, for the regions covered by the OCO-2 satellite, validation was conducted by comparing the XCO_2 concentrations deduced from the WRF-Chem results with those of OCO-2.

Figure 9a shows the time series of the simulated and observed XCO_2 concentrations. Compared to the OCO-2 XCO_2 concentrations, the simulated XCO_2 concentrations in all experiments showed similar trends but slightly overestimated values at most times. Figure 9b shows the bias of the simulated XCO_2 concentrations with respect to the OCO-2 XCO_2 concentrations. Due to the overestimated simulated XCO_2 concentrations (Fig. 9a), all six experiments showed mostly positive biases during March 2018 (Fig. 9b), with an average bias of 0.14 ppm (Table 8). Among the six experiments, ERA_Da showed the smallest bias (0.05 ppm) followed by ERA_Li (0.14 ppm) and FNL_Li (0.16 ppm) (Table 8). Similar to the biases smaller than 1 ppm (i.e., average 0.14 ppm), the average RMSE of the simulated XCO_2 concentrations with respect to OCO-2 XCO_2 concentrations for the six experiments was smaller than 1 ppm (i.e., average 0.61 ppm) (Table 8), indicating that all experiments

Table 7 Bias and RMSE of the simulated surface CO_2 concentrations for each experiment and CT2019 with respect to the observed surface CO_2 concentrations at surface CO_2 observation sites

		FNL_US	FNL_Li	FNL_Da	ERA_US	ERA_Li	ERA_Da	CT2019
Bias [ppm]	DDR	-0.693	-1.289	-2.460	-1.028	-1.535	-2.680	4.098
	KIS	1.501	0.589	-1.296	1.420	0.563	-1.418	3.964
	RYO	-0.567	-0.784	-1.469	-0.642	-0.846	-1.526	1.695
	YON	0.305	0.108	-0.278	0.210	0.044	-0.316	3.073
	AMY	-4.210	-4.296	-5.675	-4.221	-4.235	-5.619	9.205
	GSN	-2.349	-2.432	-3.335	-2.352	-2.461	-3.293	1.104
	UL	-2.227	-2.295	-2.817	-2.237	-2.287	-2.818	2.878
	Average	-1.177	-1.485	-2.476	-1.264	-1.537	-2.524	3.717
RMSE [ppm]	DDR	4.660	5.102	5.826	4.728	5.174	5.948	6.141
	KIS	4.937	4.127	3.877	4.739	3.992	3.870	6.536
	RYO	1.748	1.932	2.653	1.684	1.918	2.644	2.901
	YON	1.567	1.554	1.774	1.535	1.525	1.757	3.790
	AMY	6.687	6.411	7.470	6.747	6.415	7.421	11.019
	GSN	3.788	3.700	4.666	3.682	3.670	4.539	2.571
	UL	3.040	3.144	3.777	2.986	3.066	3.771	5.293
	Average	3.775	3.710	4.292	3.729	3.680	4.279	5.464

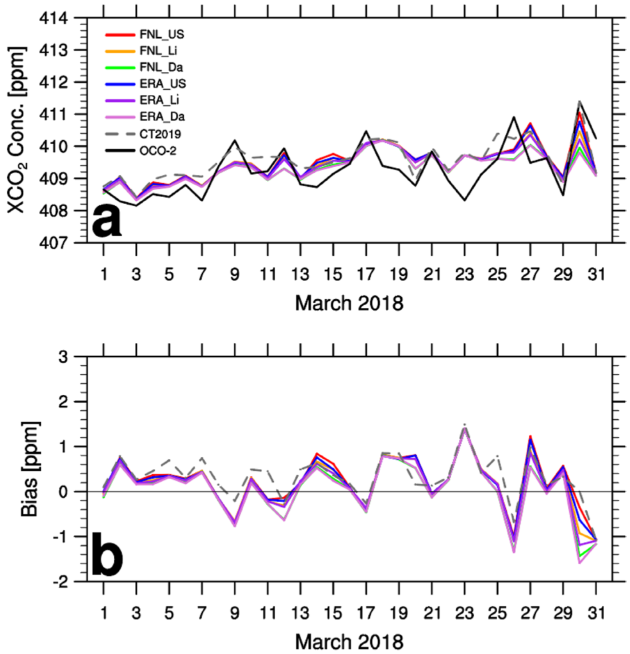

Fig. 9 Time series of **a** simulated XCO_2 and OCO-2 XCO_2 concentration (ppm) for each experiment and **b** bias (ppm) of the simulated XCO_2 concentration for each experiment with respect to the observed OCO-2 XCO_2 concentration during March 2018 (FNL_US: red solid, FNL_Li: orange solid, FNL_Da: green solid, ERA_US: blue solid, ERA_Li: purple solid, ERA_Da: light purple solid, CT2019: grey dashed, OCO-2 XCO_2: black solid)

simulated XCO_2 concentrations similar to those observed by OCO-2. FNL_Li showed the smallest RMSE of 0.59 ppm, followed by ERA_US (0.60 ppm), ERA_Li (0.60 ppm), and FNL_US (0.61 ppm) (Table 8). The slightly smaller RMSE of FNL_Li compared to that of ERA_Li may be associated with a slightly smaller RMSE of wind speed and direction in FNL_exp compared to that in ERA_exp in the entire atmosphere, as shown in Table 6. Because the column-averaged XCO_2 concentrations are mainly affected by transport in the whole atmosphere, the slightly smaller RMSE of the simulated wind fields in the whole atmosphere in the FNL_exp seems to affect the simulated XCO_2 concentrations.

Figure 10 shows the spatial distribution of the RMSE over $1° \times 1°$ bins for March 2018. The RMSE was calculated only for the bins with 20 or more observations. The RMSEs of all six experiments were similar in northern China and Japan. The greatest RMSE differences among the six experiments were in central China, where the differences in surface biogenic CO_2 concentrations among the experiments were the greatest, as shown in Fig. 3. The RMSEs in central China were relatively small in FNL_Li, ERA_US, ERA_Li, and FNL_US (Fig. 10c, b, d, and a), where the surface biogenic CO_2 absorption in these three experiments was underestimated compared to the average biogenic CO_2 absorption of all experiments (Fig. 3e, d, f, and c). Therefore, the smaller biogenic CO_2 absorption in central China in FNL_Li, ERA_Li, FNL_US, and ERA_US compared to that in other experiments resulted in a smaller RMSE over the region.

The smallest RMSE of FNL_Li implies that FNL_Li can simulate XCO_2 concentrations similar to OCO-2 XCO_2 concentrations.

4 Summary and conclusions

In this study, a high-resolution regional WRF-Chem model was used to simulate atmospheric CO_2 concentrations in East Asia, where there is high uncertainty in estimating atmospheric CO_2 concentrations. To estimate atmospheric CO_2 concentrations over East Asia appropriately, the effects of atmospheric conditions and the VPRM parameters used for simulating biogenic CO_2 concentrations were evaluated using high-resolution WRF-Chem. Various experiments were performed to evaluate the effects of experimental settings on estimating atmospheric CO_2 concentration.

The atmospheric CO_2 concentration is more affected by wind than other meteorological variables. Thus, the wind speed and direction need to be accurately simulated to simulate appropriate CO_2 concentrations. To examine the atmospheric field that simulates the wind field more accurately, FNL and ERA5 were considered as the initial and boundary conditions of WRF-Chem. In addition, the VPRM parameters that simulate biogenic CO_2 concentrations need to be appropriate for estimating atmospheric CO_2 concentrations.

To evaluate the effects of the atmospheric field and VPRM parameters on simulating surface CO_2 concentrations, six experiments were performed by using two atmospheric reanalysis fields (FNL and ERA5) and three VPRM tables (US, Li, and Dayalu tables) for March 2018 over East Asia.

The simulated surface biogenic and total CO_2 concentrations were more affected by differences in the VPRM tables

Table 8 Bias and RMSE of the simulated XCO_2 concentration for each experiment and CT2019 with respect to the observed OCO-2 XCO_2 concentrations

	FNL_US	FNL_Li	FNL_Da	ERA_US	ERA_Li	ERA_Da	CT2019
Bias [ppm]	0.224	0.164	0.058	0.194	0.142	0.045	0.324
RMSE [ppm]	0.605	0.593	0.619	0.598	0.600	0.629	0.589

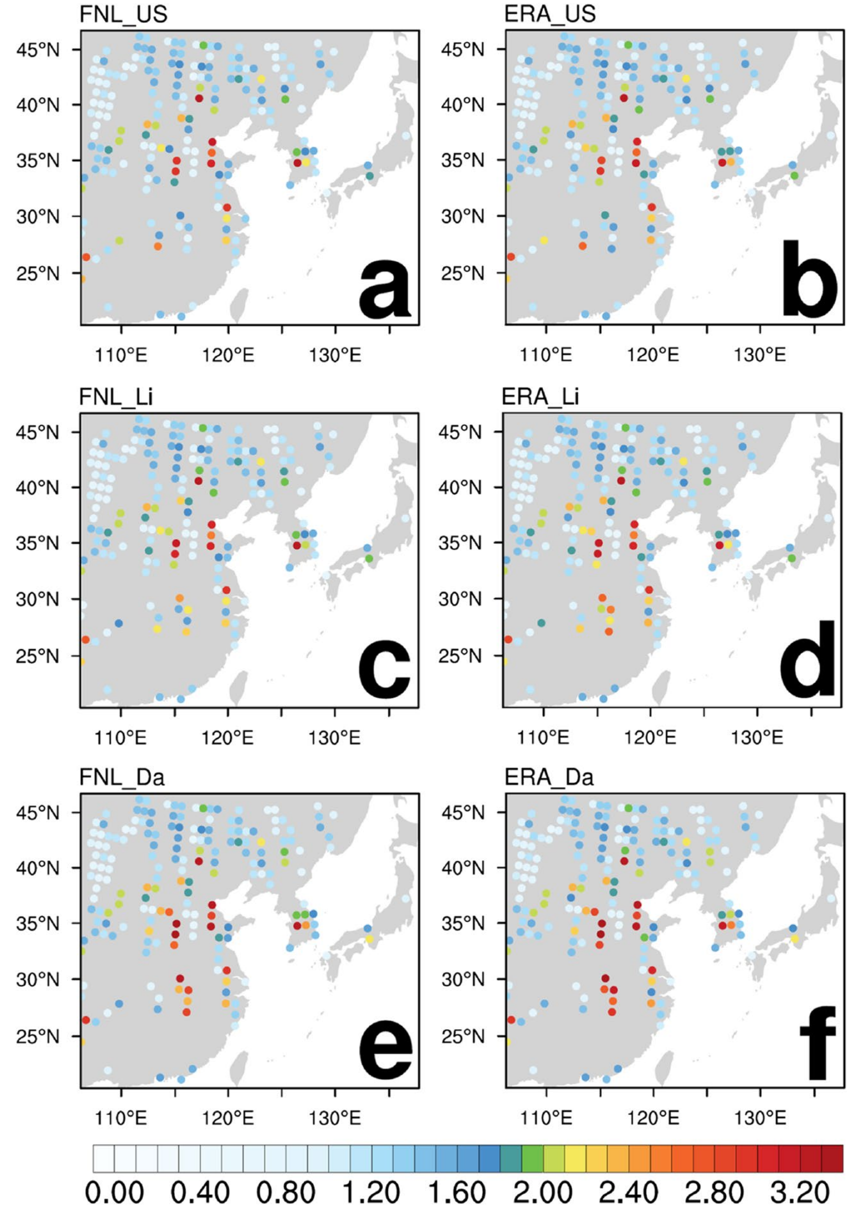

Fig. 10 Distribution of RMSE (ppm) of simulated XCO_2 concentration over $1° \times 1°$ bins in **a** FNL_US, **b** ERA_US, **c** FNL_Li, **d** ERA_Li, **e** FNL_Da, and **f** ERA_Da with respect to the observed OCO-2 XCO_2 concentration

than those in atmospheric initial and boundary conditions. Similar spatial distributions and magnitudes of surface biogenic CO_2 concentrations were observed between experiments using different atmospheric initial and boundary conditions but the same VPRM table, whereas experiments using the same atmospheric initial and boundary conditions but different VPRM tables showed distinctly different spatial distributions and magnitudes. In terms of region, the differences in surface biogenic CO_2 concentrations among the experiments were large over central China and the Korean peninsula. Since the vertical mixing also affects CO_2 concentrations, the effect of physical parameterizations on the vertical mixing and simulation of CO_2 concentrations over Asia would be a future work.

To verify the accuracy of the simulated wind and CO_2 concentrations, they were compared with observed values. From surface and pressure level validations, all experiments using FNL as the initial and boundary conditions (FNL_exp) were slightly more accurate in wind speed and direction forecasts than those using ERA5 as the initial and boundary conditions (ERA_exp) for the experimental period over East Asia. From the validation of surface CO_2 concentrations, on average, the experiments that used either ERA or FNL as the initial and boundary conditions with the Li table as the VPRM table in WRF-Chem showed smaller biases and RMSEs than the other four experiments and also showed much smaller biases and RMSEs compared to CT2019. Therefore, among the six experiments, ERA_Li and FNL_Li simulated surface CO_2 concentrations closest to the observed values. From the validation of XCO_2 concentrations, FNL_Li using FNL as the initial and boundary conditions and the Li table as the VPRM table in WRF-Chem showed smaller biases and RMSEs than other experiments. Based on all validations of wind and CO_2 concentrations, the combination of FNL as the atmospheric initial and boundary conditions and Li table as the VPRM table showed the overall best performance and was thus most suitable for simulating atmospheric CO_2 concentrations using WRF-Chem during the experimental period for East Asia.

In future studies, using the WRF-Chem configurations based on the FNL and Li table, high-resolution atmospheric CO_2 concentrations over East Asia will be simulated for longer periods, and the characteristics of the high-resolution regional CO_2 concentrations will be evaluated.

Acknowledgements The authors appreciate the reviewer's valuable comments. The authors acknowledge atmospheric CO_2 measurement data providers and cooperating agencies at NOAA ESRL, Center for Environmental Science in Saitama, Japan Meteorological Agency, and Korea Meteorological Administration. The authors also acknowledge the OCO-2 project at the Jet Propulsion Laboratory, California Institute of Technology, and the OCO-2 data archive maintained at the NASA Goddard Earth Science Data and Information Services Center, and CarbonTracker CT2019 results provided by NOAA ESRL.

Author contribution Min-Gyung Seo contributed to formal analysis, investigation, methodology, software, validation, visualization, and writing original draft. Hyun Mee Kim contributed to conceptualization, formal analysis, funding acquisition, investigation, methodology, project administration, providing resources, supervision, validation, and writing – review and editing. Dae-Hui Kim contributed to investigation, methodology, software, validation, and visualization.

Funding This study was supported by a National Research Foundation of Korea (NRF) grant funded by the South Korean government (Ministry of Science and ICT) (Grant 2021R1A2C1012572) and the Yonsei Signature Research Cluster Program of 2023 (2023–22-0009).

Data availability The datasets generated and analyzed during the current study are available from the corresponding author on reasonable request.

Code availability The WRF-Chem code can be downloaded from https://www2.mmm.ucar.edu/wrf/users/download/get_sources_new.php.

Declarations

Ethics declarations Not applicable.

Consent to participate Not applicable.

Consent for publication Not applicable.

Competing interests The authors declare no competing interests.

References

Ahmadov R, Gerbig C, Kretschmer R, Koerner S, Neininger B, Dolman AJ, Sarrat C (2007) Mesoscale covariance of transport and CO_2 fluxes: evidence from observations and simulations using the WRF-VPRM coupled atmosphere-biosphere model. J Geophys Res: Atmos 112(D22):D22107

Baklanov A, Schlünzen K, Suppan P, Baldasano J, Brunner D, Aksoyoglu S, Carmichael G, Douros J, Flemming J, Forkel R, Galmarini S, Gauss M, Grell G, Hirtl M, Joffre S, Jorba O, Kaas E, Kaasik M, Kallos G, Kong X, Korsholm U, Kurganskiy A, Kushta J, Lohmann U, Mahura A, Manders-Groot A, Maurizi A, Moussiopoulos N, Rao ST, Savage N, Seigneur C, Sokhi RS, Solazzo E, Solomos S, Sorensen B, Tsegas G, Vignati E, Vogel B, Zhang Y (2014) Online coupled regional meteorology chemistry models in Europe: current status and prospects. Atmos Chem Phys 14:317–398. https://doi.org/10.5194/acp-14-317-2014

Ballav S, Patra PK, Takigawa M, Ghosh S, De UK, Maksyutov S, Murayama S, Mukai H, Hashimoto S (2012) Simulation of CO_2 concentration over East Asia using the regional transport model WRF-CO_2. J Meteorol Soc Japan Ser II 90(6):959–976

Ballav S, Naja M, Patra PK, Machida T, Mukai H (2020) Assessment of spatio-temporal distribution of CO_2 over greater Asia using the WRF-CO_2 model. J Earth Syst Sci 129(1):1–16. https://doi.org/10.1007/s12040-020-1352-x

Chen HW, Zhang F, Lauvaux T, Davis KJ, Feng S, Butler MP, Alley RB (2019) Characterization of regional-scale CO_2 transport uncertainties in an ensemble with flow-dependent transport errors. Geophys Res Lett 46(7):4049–4058

Cho M, Kim HM (2022) Effect of assimilating CO2 observations in the Korean Peninsula on the inverse modeling to estimate surface CO_2 flux over Asia. PLoS One 17:e0263925. https://doi.org/10.1371/journal.pone.0263925

Connor BJ, Boesch H, Toon G, Sen B, Miller C, Crisp D (2008) Orbiting Carbon Observatory: inverse method and prospective error analysis. J Geophys Res: Atmos 113(D5). https://doi.org/10.1029/2006JD008336

Dayalu A, Munger JW, Wofsy SC, Wang Y, Nehrkorn T, Zhao Y, McElroy MB, Nielsen CP, Luus K (2018) Assessing biotic contributions to CO_2 fluxes in northern China using the Vegetation, Photosynthesis and Respiration Model (VPRM-CHINA) and observations from 2005 to 2009. Biogeosciences 15(21):6713

Dee DP, Uppala SM, Simmons AJ, Berrisford P, Poli P, Kobayashi S, Andrae U, Balmaseda MA, Balsamo G, Bauer P, Bechtold P, Beljaars ACM, van de Berg L, Bidlot J, Bormann N, Delsol C, Dragani R, Fuentes M, Geer AJ, Haimberger L, Healy SB, Hersbach H, Hólm EV, Isaksen L, Kållberg P, Köhler M, Matricardi M, Mcnally AP, Monge-Sanz BM, Morcrette J-J, Park B-K, Peubey C, de Rosnay P, Tavolato C, Thépaut J-N, Vitart F (2011) The

ERA-Interim reanalysis: configuration and performance of the data assimilation system. Q J R Meteorol Soc 137:553–597

Díaz-Isaac LI, Lauvaux T, Davies KJ (2018) Impact of physical parameterizations and initial conditions on simulated atmospheric transport and CO_2 mole fractions in the US Midwest. Atmos Chem Phys 18:14813–14835. https://doi.org/10.5194/acp-18-14813-2018

Dong X, Yue M, Jiang Y, Hu X-M, Ma Q, Pu J, Zhou G (2021) Analysis of CO_2 spatio-temporal variations in China using a weather–biosphere online coupled model. Atmos Chem Phys 21:7217–7233. https://doi.org/10.5194/acp-21-7217-2021

European Commission (2011) Emission database for global atmospheric research (EDGAR), release version 4.2. Technical report, Joint Research Centre (JRC)/Netherlands Environmental Assessment Agency (PBL). http://edgar.jrc.ec.europa.eu/. Accessed 28 June 2020

Feng L, Palmer PI, Parker RJ, Deutscher NM, Feist DG, Kivi IM, Sussmann R (2016) Estimates of European uptake of CO_2 inferred from GOSAT XCO_2 retrievals: sensitivity to measurement bias inside and outside Europe. Atmos Chem Phys 16(3):1289–1302

Feng S, Lauvaux T, Davis KJ, Keller K, Zhou Y, Williams C, Schuh AE, Liu J, Baker I (2019) Seasonal characteristics of model uncertainties from biogenic fluxes, transport, and large-scale boundary inflow in atmospheric CO_2 simulations over North America. J Geophysical Res: Atmos 124(24):14325–14346

Friedlingstein P, Jones MW, O'Sullivan M, Andrew RM, Bakker DCE, Hauck J, Quéré CL, Peters GP, Peters W, Pongratz J, Sitch S, Canadell JG, Ciais P, Jackson RB, Alin SR, Anthoni P, Bates NR, Becker M, Bellouin N, Bopp L, Chau TTT, Chevallier F, Chini LP, Cronin M, Currie KI, Decharme B, Djeutchouang LM, Dou X, Evans W, Feely RA, Feng L, Gasser T, Gilfillan D, Gkritzalis T, Grassi G, Gregor L, Gruber N, Gürses Ö, Harris I, Houghton RA, Hurtt GC, Iida Y, Ilyina T, Luijkx IT, Jain A, Jones SD, Kato E, Kennedy D, Goldewijk KK, Knauer J, Korsbakken JI, Körtzinger A, Landschützer P, Lauvset SK, Lefèvre N, Lienert S, Liu J, Marland G, McGuire PC, Melton JR, Munro DR, Nabel JEMS, Nakaoka S-I, Niwa Y, Ono T, Pierrot D, Poulter B, Rehder G, Resplandy L, Robertson E, Rödenbeck C, Rosan TM, Schwinger J, Schwingshackl C, Séférian R, Sutton AJ, Sweeney C, Tanhua T, Tans PP, Tian H, Tilbrook B, Tubiello F, van der Werf GR, Vuichard N, Wada C, Wanninkhof R, Watson AJ, Willis D, Wiltshire AJ, Yuan W, Yue C, Yue X, Zaehle S, Zeng J (2022) Global carbon budget 2022. Earth Syst Sci Data 14(11):4811–4900

Grell GA, Dévényi D (2002) A generalized approach to parameterizing convection combining ensemble and data assimilation techniques. Geophys Res Lett 29:1693. https://doi.org/10.1029/2002GL015311

Grell GA, Peckham SE, Schmitz R, McKeen SA, Frost G, Skamarock WC, Eder B (2005) Fully coupled "online" chemistry within the WRF model. Atmos Environ 39(37):6957–6975

Hersbach H, Bell B, Berrisford P, Biavati G, Horányi A, Muñoz SJ, Nicolas J, Peubey C, Radu R, Rozum I, Schepers D, Simmons A, Soci C, Dee D, Thépaut J-N (2018) ERA5 hourly data on pressure levels from 1979 to present. Copernicus Climate Change Service (C3S) Climate Data Store (CDS). (Accessed on < 07-July-2021 >), https://doi.org/10.24381/cds.bd0915c6

Hilton TW, Davis KJ, Keller K, Urban NM (2013) Improving North American terrestrial CO_2 flux diagnosis using spatial structure in land surface model residuals. Biogeosciences 10(7):4607

Hong SY, Lim JO (2006) The WRF single–moment 6–class microphysics scheme (WSM6). Asia-Pac J Atmos Sci 42:129–151

Hong S-Y, Noh Y, Dudhia J (2006) A new vertical diffusion package with an explicit treatment of entrainment processes. Mon Weather Rev 134:2318–2341

Hu XM, Crowell S, Wang Q, Zhang Y, Davis KJ, Xue M, Xiao X, Moore B, Wu X, Choi Y, DiGangi JP (2020) Dynamical Downscaling of CO2 in 2016 over the contiguous United States using WRF-VPRM, a weather-biosphere-online-coupled model. J Adv Model Earth Syst 12(4):e2019MS001875

Iacono MJ, Delamere JS, Mlawer EJ, Shephard MW, Clough SA, Collins WD (2008) Radiative forcing by long-lived greenhouse gases: calculations with the AER radiative transfer models. J Geophys Res: Atmos 113:D13103

Iida Y, Takatani Y, Kojima A, Ishii M (2021) Global trends of ocean CO_2 sink and ocean acidification: an observation-based reconstruction of surface ocean inorganic carbon variables. J Oceanogr 77:323–358

Jacobson AR et al (2020) CarbonTracker CT2019. NOAA Earth System Research Laboratory, Global Monitoring Division. https://doi.org/10.25925/39M3-6069

Jiménez PA, Dudhia J, González-Rouco JF, Navarro J, Montávez JP, García-Bustamante E (2012) A revised scheme for the WRF surface layer formulation. Mon Weather Rev 140:898–918. https://doi.org/10.1175/MWR-D-11-00056.1

Jing Y, Wang T, Zhang P, Chen L, Xu N, Ma Y (2018) Global atmospheric CO_2 concentrations simulated by GEOS-Chem: comparison with GOSAT, carbon tracker and ground-based measurements. Atmosphere 9(5):175

Jung M, Henkel K, Herold M, Churkina G (2006) Exploiting synergies of global land cover products for carbon cycle modeling. Remote Sens Environ 101(4):534–553

Kanamitsu M, Ebisuzaki W, Woollen J, Yang SK, Hnilo JJ, Fiorino M, Potter GL (2002) Ncep–doe amip-ii reanalysis (r-2). Bull Am Meteor Soc 83(11):1631–1644

Kim HM, Kim D-H (2021) Effect of boundary conditions on adjoint-based forecast sensitivity observation impact in a regional model. J Atmos Oceanic Tech 38:1233–1247. https://doi.org/10.1175/JTECH-D-20-0040.1

Kim J, Kim HM, Cho CH (2014a) Influence of CO_2 observations on the optimized CO_2 flux in an ensemble Kalman filter. Atmos Chem Phys 14:13515–13530. https://doi.org/10.5194/acp-14-13515-2014

Kim J, Kim HM, Cho CH (2014b) The effect of optimization and the nesting domain on carbon flux analyses in Asia using a carbon tracking system based on the ensemble Kalman filter. Asia-Pac J Atmos Sci 50:327–344. https://doi.org/10.5194/acp-14-13515-2014

Kim J, Kim HM, Cho C-H, Boo K-O, Jacobson AR, Sasakawa M, Machida T, Arshinov M, Fedoseev N (2017) Impact of Siberian observations on the optimization of surface CO_2 flux. Atmos Chem Phys 17:2881–2899. https://doi.org/10.5194/acp-17-2881-2017

Kim H, Kim HM, Kim J, Cho CH (2018) Effect of data assimilation parameters on the optimized surface CO_2 flux in Asia. Asia-Pac J Atmos Sci 54(1):1–17. https://doi.org/10.1007/s13143-017-0049-9

Li R, Zhang M, Chen L, Kou X, Skorokhod A (2017) CMAQ simulation of atmospheric CO_2 concentration in East Asia: comparison with GOSAT observations and ground measurements. Atmos Environ 160:176–185

Li X, Hu XM, Ma Y, Wang Y, Li L, Zhao Z (2019) Impact of planetary boundary layer structure on the formation and evolution of air-pollution episodes in Shenyang, Northeast China. Atmos Environ 214:116850

Li X, Hu XM, Cai C, Jia Q, Zhang Y, Liu J, Xue M, Xu J, Wen R, Crowell SMR (2020) Terrestrial CO_2 fluxes, concentrations, sources and budget in Northeast China: Observational and modeling studies. J Geophys Res: Atmos 125(6):e2019JD031686

Liu Y, Yue T, Zhang L, Zhao N, Zhao M, Liu Y (2018) Simulation and analysis of XCO_2 in North China based on high accuracy surface modeling. Environ Sci Pollut Res 25(27):27378–27392

Mahadevan P, Wofsy SC, Matross DM, Xiao X, Dunn AL, Lin JC, Gerbig C, Munger JW, Chow VY, Gottlieb EW (2008) A satellite-based biosphere parameterization for net ecosystem CO2 exchange: Vegetation Photosynthesis and Respiration Model

(VPRM). Global Biogeochem Cycles 22(2):GB2005. https://doi.org/10.1029/2006GB002735
Martin CR, Zeng N, Karion A, Mueller K, Ghosh S, Lopez-Coto I, Gurney KR, Oda T, Prasad K, Liu Y, Dickerson RR, Whetstone J (2019) Investigating sources of variability and error in simulations of carbon dioxide in an urban region. Atmos Environ 199:55–69
Mesinger F, DiMego G, Kalnay E, Mitchell K, Shafran PC, Ebisuzaki W, Jović D, Woollen J, Rogers E, Berbery EH, Ek MB, Fan Y, Grumbine R, Higgins W, Li H, Lin Y, Manikin G, Parrish D, Shi W (2006) North American regional reanalysis. Bull Am Meteor Soc 87(3):343–360
Moran D, Kanemoto K, Jiborn M, Wood R, Többen J, Seto KC (2018) Carbon footprints of 13000 cities. Environ Res Lett 13:064041. https://doi.org/10.1088/1748-9326/aac72a
Nasrallah HA, Balling RC Jr, Madi SM, Al-Ansari L (2003) Temporal variations in atmospheric CO_2 concentrations in Kuwait City, Kuwait with comparisons to Phoenix, Arizona, USA. Environ Pollut 121(2):301–305
NCEP/NOAA (2000) NCEP FNL Operational Model Global Tropospheric Analyses, continuing from July 1999. Research Data Archive at the National Center for Atmospheric Research, Computational and Information Systems Laboratory, Boulder, CO. https://doi.org/10.5065/D6M043C6. Accessed 05 September 2023
Oda T, Maksyutov S (2015) ODIAC fossil fuel CO_2 emission dataset (Version name: ODIAC2019), Center for Global Environmental Research, National Institute for Environmental Studies. https://doi.org/10.17595/20170411.001. Accessed 28 June 2020.
Oda T, Maksyutov S, Andres RJ (2018) The open-source data inventory for anthropogenic CO_2, version 2016 (ODIAC2016): a global monthly fossil fuel CO_2 gridded emissions data product for tracer transport simulations and surface flux inversions. Earth Syst Sci Data 10(1):87-107. 10.5194/essd-10-87-2018. URL https://www.earth-syst-sci-data.net/10/87/2018/
O'Dell CW, Connor B, Bösch H, O'Brien D, Frankenberg C, Castano R, Christi M, Eldering D, Fisher B, Gunson M, McDuffie J, Miller CE, Natraj V, Oyafuso F, Polonsky I, Smyth M, Taylor T, Toon GC, Wennberg PO, Wunch D (2012) The ACOS CO_2 retrieval algorithm–Part 1: Description and validation against synthetic observations. Atmos Meas Tech 5(1):99–121
Osterman G, Eldering A, Avis C, Chafin B, O'Dell C, Frankenberg C, Fisher B, Mandrake L, Wunch D, Granat R, Crisp D (2018) Orbiting Carbon Observatory-2 (OCO-2) data product user's guide, operational L1 and L2 data version 8 and lite file version 9. Jet Propulsion Laboratory, Pasadena, CA, USA
Park J, Kim HM (2020) Design and evaluation of CO_2 observation network to optimize surface CO_2 fluxes in Asia using observation system simulation experiments. Atmos Chem Phys 20:5175–5195. https://doi.org/10.5194/acp-20-5175-2020
Park C, Gerbig C, Newman S, Ahmadov R, Feng S, Gurney KR, Carmichael GR, Park S-Y, Lee H-W, Goulden M, Stutz J, Peischl J, Ryerson T (2018) CO_2 transport, variability, and budget over the Southern California air basin using the high-resolution WRF-VPRM model during the CalNex 2010 Campaign. J Appl Meteorol Climatol 57(6):1337–1352
Park C, Park SY, Gurney KR, Gerbig C, DiGangi JP, Choi Y, Lee HW (2020) Numerical simulation of atmospheric CO_2 concentration and flux over the Korean Peninsula using WRF-VPRM model during Korus-AQ 2016 campaign. PLoS One 15(1):e0228106
Pillai D, Gerbig C, Ahmadov R, Rödenbeck C, Kretschmer R, Koch T, Thompson R, Neininger B, Lavrié JV (2011) High-resolution simulations of atmospheric CO_2 over complex terrain - representing the Ochsenkopf mountain tall tower. Atmos Chem Phys 11:7445–7464
Powers JG, Klemp JB, Skamarock WC, Davis CA, Dudhia J, Gill DO, Coen JL, Gochis DJ, Ahmadov R, Peckham SE, Grell GA, Michalakes J, Trahan S, Benjamin SG, Alexander CR, Dimego GJ, Wang W, Schwartz CS, Romine GS, Liu Z, Snyder C, Chen F, Barlage MJ, Yu W, Duda MG (2017) The weather research and forecasting model: overview, system efforts, and future directions. Bull Am Meteor Soc 98(8):1717–1737
Seo M-G, Kim HM (2023) Effect of meteorological data assimilation using 3DVAR on high-resolution simulations of atmospheric CO_2 concentrations in East Asia. Atmos Pollut Res 14:101759. https://doi.org/10.1016/j.apr.2023.101759
Shim C, Lee J, Wang Y (2013) Effect of continental sources and sinks on the seasonal and latitudinal gradient of atmospheric carbon dioxide over East Asia. Atmos Environ 79:853–860
Stephens BB, Gurney KR, Tans PP, Sweeney C, Peters W, Bruhwiler L, Ciais P, Ramonet M, Bousquet P, Nakazawa T, Aoki S, Machida T, Inoue G, Vinnichenko N, Lloyd J, Jordan A, Heimann M, Shibistova O, Langenfelds RL, Steele LP, Francey RJ, Denning AS (2007) Weak Northern and Strong Tropical Land Carbon Uptake from Vertical Profiles of Atmospheric CO_2. Science 316:1732–1735. https://doi.org/10.1126/science.1137004
Takatani Y, Enyo K, Iida Y, Kojima A, Nakano T, Sasano D, Kosugi N, Midorikawa T, Suzuki T, Ishii M (2014) Relationships between total alkalinity in surface water and sea surface dynamic height in the Pacific Ocean. J Geophys Res: Oceans 119(5):2806–2814
Tewari M, Chen F, Wang W, Dudhia J, LeMone MA, Mitchell K, Ek M, Gayno G, Wegiel J, Cuenca RH (2004) Implementation and verification of the unified NOAH land surface model in the WRF model. 20th conference on weather analysis and forecasting/16th conference on numerical weather prediction (Vol. 1115). Seattle, WA: American Meteorological Society
Xiao X, Hollinger D, Aber J, Goltz M, Davidson EA, Zhang Q, Moore B III (2004) Satellite-based modeling of gross primary production in an evergreen needleleaf forest. Remote Sens Environ 89(4):519–534
Zhao X, Marshall J, Hachinger S, Gerbig C, Frey M, Hase F, Chen F (2019) Analysis of total column CO_2 and CH_4 measurements in Berlin with WRF-GHG. Atmos Chem Phys 19(17):11279–11302
Zheng T, Nassar R, Baxter M (2019) Estimating power plant CO_2 emission using OCO-2 XCO_2 and high resolution WRF-Chem simulations. Environ Res Lett 14(8):085001
Zheng B, Chevallier F, Ciais P, Broquet G, Wang Y, Lian J, Zhao Y (2020) Observing carbon dioxide emissions over China's cities and industrial areas with the Orbiting Carbon Observatory-2. Atmos Chem Phys 20(14):8501–8510